RESEARCH ARTICLE

ADVANCED FUNCTIONAL MATERIALS
www.afm-journal.de

Metaverse-Enabled Yoga Coach Avatar Using AI-Enhanced Multimodal Insole Sensing System

*Luwei Wang, Xinge Guo, Zixuan Zhang, and Chengkuo Lee**

Plantar biomechanical monitoring has emerged as an indispensable tool for health assessment and activity recognition. However, existing insole systems lack the capability to support multimodal sensing for sports monitoring due to limitations in materials and complexity of system design. Hydrogel, owing to its multimodal sensing capabilities and biocompatible properties, showcases great potential for advanced plantar monitoring during exercise. Here, the study proposes an artificial intelligence (AI)-enhanced multimodal insole sensing system (AEIS) based on ionic hydrogel for immersive, real-time posture correction and personalized yoga training guidance. The AEIS integrates a 32-channel hydrogel-based sensing array with a customized wireless circuit, enabling simultaneous monitoring of plantar pressure, temperature, and sweat. By leveraging hybrid AI algorithms, AEIS serves as a virtual yoga coach, achieving high accuracy in posture recognition (98.33%) and imbalance detection (90.06%). Furthermore, the developed approach based on random forest (RF) is trained on center-of-pressure (COP) stability data from yoga coach, enabling AEIS to analyze real-time data of yoga practitioners and deliver personalized posture guidance. Meanwhile, the embedded haptic units provide real-time haptic feedback in response to improper plantar pressure distribution. AEIS forms an interactive metaverse-based yoga training platform, offering users an immersive, face-to-face-like experience with a virtual yoga coach.

1. Introduction

As society and the economy rapidly evolve, the importance of wearable electronic devices integrated with artificial intelligence (AI)-driven data analytics has grown significantly in the era of the Internet of Things (IoT).[1–6] Recent advances in materials science, fabrication technologies, and system integration have enabled wearable sensing systems capable of real-time, continuous, and personalized monitoring,[7–14] demonstrating broad potential in health monitoring, human activity recognition, virtual reality/ augmented reality (VR/AR) haptic interactions, and human-machine interfaces.[15–21] To date, significant efforts have been made to develop wearable sensors tailored for healthcare applications, including physical activity monitoring, vital signs measurement, and biometric information collection.[22–24] With increasing demand for comprehensive physiological insights, multimodal sensing systems have emerged to collect diverse signals simultaneously. However, integrating multiple sensor modules often leads to drawbacks such as increased circuit complexity, larger device footprints, and elevated power consumption.[25] To overcome these challenges, developing multifunctional materials capable of simultaneously detecting multiple signals is of great significance.[26,27] Among these, hydrogels stand out for their excellent biocompatibility, mechanical flexibility, and ionic conductivity, making them promising candidates for next-generation wearable interfaces that ensure long-term skin conformity and multimodal signal detection.[28–31]

Over the past few decades, wearable sensing systems have predominantly focused on health monitoring and human activity recognition. However, recent advancements in sensing mechanisms and smart materials now allow wearable devices to support posture correction, exercise intensity assessment, training feedback, and performance optimization.[32–36,24] Comprehensive data on individual physical fitness and athletic performance are essential not only for advancing the understanding of human physiology but also for enabling intelligent, data-driven coaching. Recent studies have highlighted the potential of wearable sensor systems in providing real-time feedback and enhancing sports coaching. For instance, Y. Ma et al. reported a tactile-tension sensor capable of recognizing complex combat motions during

---

L. Wang, X. Guo, Z. Zhang, C. Lee
Department of Electrical & Computer Engineering
National University of Singapore
4 Engineering Drive 3, Singapore 117576, Singapore
E-mail: elelc@nus.edu.sg

L. Wang, X. Guo, Z. Zhang, C. Lee
Center for Intelligent Sensors and MEMS (CISM)
National University of Singapore
5 Engineering Drive 1, Singapore 117608, Singapore

C. Lee
National University of Singapore Suzhou Research Institute (NUSRI)
Suzhou 215123, China

C. Lee
NUS Graduate School – Integrative Sciences and Engineering Program (ISEP)
National University of Singapore
Singapore 119077, Singapore

The ORCID identification number(s) for the author(s) of this article can be found under https://doi.org/10.1002/adfm.202519562

DOI: 10.1002/adfm.202519562

taekwondo training.[37] Z. Guo et al. developed a multidimensional motion sensor system for monitoring waist and gait movements in football, integrating it into immersive VR applications.[38] S. Gao et al. introduced a ratchet-based triboelectric nanogenerator (TENG) for lower-limb motion monitoring, enabling players to control virtual ball movements through real-time physical input.[39] Such capabilities are particularly valuable for structured physical activities like yoga, which has gained worldwide popularity due to its benefits in improving flexibility, core strength, balance, and mental well-being.[40–42] Despite these advantages, the efficacy of yoga practice depends critically on proper posture execution, as incorrect poses may result in muscle strain, joint injury, or long-term biomechanical dysfunction.[43] Therefore, traditional yoga practice is typically guided by trained instructors to ensure safety and effectiveness. However, with growing interest in remote and self-guided practices, numerous studies have proposed technology-assisted yoga recognition systems using infrared sensors, camera-based pose estimation, and inertial measurement units (IMUs) to automate posture classification.[44–46] While these systems have achieved high recognition accuracy by analyzing features such as joint angles and motion speed (Table S1 and Text S1, Supporting Information),[47–55] they are always constrained by environmental sensitivity (e.g., lighting and occlusion), privacy concerns in domestic settings, and user burden due to the need for multi-sensor wearables, as well as the inability to fully reflect internal biomechanical performance. In particular, current approaches often neglect crucial physiological indicators such as center-of-pressure (COP) dynamics and plantar pressure distribution, which are essential for assessing postural stability, balance control, and muscle engagement during yoga poses.[56–58]

Plantar pressure distribution analysis provides valuable biomechanical insights into yoga practice, particularly concerning weight distribution, postural stability, and balance. Monitoring spatiotemporal plantar pressure changes enables the detection of subtle COP shifts and imbalance patterns that cannot be captured by cameras or IMUs alone. In addition, the foot, as a vital support structure for human movement, allows early disease detection, health assessments, and activity recognition through gait abnormalities and plantar pressure analysis.[59–62] Neurological disorders, orthopedic conditions, and metabolic diseases, such as flat foot, high arched foot, pronated foot, supinator foot,[63–65] Parkinson's disease,[66–68] and diabetic foot,[69] can lead to gait abnormalities and alter plantar pressure distribution. The growing interest in wearable devices for gait and movement monitoring, combined with advancements in AI analytics, has prompted research into real-time plantar pressure detection based on various transduction mechanisms (Table S2 and Text S2, Supporting Information), including capacitive,[28,30,69–73] resistive,[61,74,75] piezoresistive,[75] triboelectric,[62,76,77] and piezoelectric.[11,78] Capacitive and resistive sensors, however, require external power, increasing complexity and limiting suitability for long-term monitoring. Self-powered triboelectric and piezoelectric sensors, though beneficial, predominantly capture dynamic signals and are less effective for static or prolonged monitoring.[8] Additionally, current plantar sensors frequently utilize non-degradable materials with poor biocompatibility, limiting their integration into long-term wearable systems. Hydrogels, in contrast, offer long-term softness, high ionic conductivity, and compatibility with skin contact, making them particularly attractive for constructing multifunctional insoles capable of multimodal sensing (Table S3 and Text S3, Supporting Information).[79] By incorporating physiological indicators such as skin temperature and sweat secretion, the hydrogel-based insole provides deeper insights into exercise intensity, fatigue, and user comfort. Furthermore, with recent advances in VR/AR and the artificial intelligence of things (AIoT),[79–84] user interaction paradigms are shifting toward AI-driven coaching systems that surpass basic posture recognition or human-dependent instruction. Hydrogel-based plantar sensing has emerged as a promising approach for advanced yoga coaching systems, delivering comprehensive multimodal physiological and biomechanical data crucial for posture, balance, and intensity evaluation.

Herein, we present the AI-enhanced multimodal insole sensing system (AEIS) integrating a multifunctional hydrogel-based smart insole, a metaverse-enhanced yoga coach avatar, and a haptic feedback array to deliver immersive real-time posture correction and personalized yoga training guidance through the digital twin. The self-powered multimodal insole sensing platform employs polyvinyl alcohol (PVA)/ polyacrylamide (PAAm)/ lithium chloride (LiCl)/ glycerol (Gly) ionic hydrogel (**Figure 1**). This platform features a 32-channel hydrogel-based sensor array for plantar pressure, temperature, and sweat monitoring, alongside embedded vibrators for precise haptic feedback. Leveraging IoT modules and machine learning algorithms, the system robustly classifies 15 yoga postures and assesses imbalance during prolonged posture maintenance. Furthermore, the AEIS supports multi-user adaptive coaching, offering user identification and personalized guidance. A regression model trained on expert COP trajectories predicts user-specific stability parameters from dynamic plantar pressure distributions. By comparing the predicted COP-based stability parameters with user performance, the system then provides real-time, personalized corrective guidance. In addition, haptic feedback is provided through vibration while incorrect pressure distribution is detected. A metaverse-enabled yoga coach avatar is then built within a VR/AR environment, where the avatar interacts with the users to offer personalized guidance and corrections based on the sensor data. Simultaneously, a digital twin of the user is visualized to reflect their actual posture, enabling intuitive comparison and interactive feedback throughout the training process. An AI-enhanced yoga training paradigm is established, integrating multimodal sensing, multi-user yoga training, and haptic feedback into an immersive yoga coaching ecosystem. This system effectively bridges the physical and virtual domains, enhancing user experience and the effectiveness of yoga learning.

2. Results and Discussion

2.1. Multimodal Sensing Capability of the AEIS for Comprehensive Monitoring

The system architecture of AEIS for building a metaverse-enabled yoga coach avatar is illustrated in Figure 1. As shown in Figure 1a, the hydrogel-based insole achieves multifunctional sensing, including pressure, temperature, and sweat monitoring, with the hydrogel consisting of a double-network structure

Figure 1. An Overview of the Metaverse-Enabled Yoga Coach Avatar with AEIS. a) Multimodal sensing functionality achieved by PVA/ PAAm/ LiCl/ Gly hydrogel-based self-powered sensors. b) The structure of the PVA/ PAAm/ LiCl/ Gly hydrogel-based sensor. c) The detailed structure diagram of the multimodal insole sensing system. d) Illustration of the metaverse virtual space for personalized yoga guidance, health status monitoring, and posture correction.

composed of PVA/PAAm and LiCl as the ionic source (Figure 1b). Figure 1c depicts the schematic of the self-powered multimodal intelligent insole system, where four vibrators and a wireless communication circuit are embedded within the bottom PLA encapsulation. Above the PLA encapsulation layer, an array of 32 silver electrodes, fabricated on a flexible printed-circuit board (FPCB) with a polyimide (PI) substrate, is positioned (cross section of the insole system is provided in Figure S1, Supporting Information). The hydrogel sensing layer (Figure S2, Supporting Information) is placed between the silver electrode array and the aluminum layer, forming a sandwiched structure (Figure S3, Supporting Information and Experimental Section). A thin insulating layer above the aluminum electrodes ensures electrical isolation. With the silver and aluminum electrodes, ions are attracted to both electrodes, generating an open circuit voltage. This configuration facilitates self-sustained signal generation.

At the system level, real-time sensory data during yoga practice are collected by a customized miniaturized printed circuit board (PCB) (Figure S4, Supporting Information and Experimental Section) and wirelessly transmitted to an AI-enabled cloud server.

Using various machine learning algorithms, analyses of plantar pressure distributions during yoga facilitate posture recognition, imbalance status detection, and multi-user training. A digital twin of the user is built by projecting multimodal data from the physical space into the virtual space, and the metaverse-enabled yoga coach avatar is established to offer personalized guidance for users (Figure 1d). The AEIS also aids different users in adjusting their plantar pressure distribution via haptic feedback from vibrators strategically positioned at the forefoot, heel, and the left and right sides of the insole. By linking the virtual yoga coach in the metaverse with real-time perception of users, the AEIS allows users to receive immersive, interactive, and face-to-face-like yoga training experiences. Comprehensive assessment of physical performance during exercise relies on multimodal sensing to capture key physiological and biomechanical signals. Prior studies predominantly focused on pressure monitoring, neglecting rich multimodal plantar data during human activities. Operational principles and designation for multimodal sensing are illustrated in **Figure 2**a. For pressure and temperature sensing (Figure 2a(i),(ii)), LiCl is used as the ionic source, while aluminum and silver electrodes form a sandwich structure around the hydrogel. Driven by the distinct redox potentials of the two electrodes, ions (e.g., H^+, Li^+, and Cl^-) in the hydrogel are drawn to participate in reactions, thereby establishing a self-sustained, stable potential without external power.[79,85] Electrons flow from silver to aluminum electrodes, creating an electric current. The total resistance of the sensor consists of electrode-hydrogel contact resistance and intrinsic hydrogel resistance. When an external force is applied to the sensor, the contact resistance between the electrodes and the hydrogel decreases, leading to an increase in the output voltage, while a temperature rise enhances ion mobility within the hydrogel, thereby decreasing the intrinsic resistance and promoting an increase in output voltage. For sweat sensing (Figure 2a(iii)), the electrodes are configured at the bottom, leaving the hydrogel surface available for direct skin contact and sweat detection. Different from the hydrogel layer used for force and temperature sensing, the hydrogel for sweat sensing is fabricated without LiCl, resulting in no initial open-circuit voltage. When sweat appears and is absorbed by the hydrogel layer, ions from the sweat (e.g., Na^+, Cl^-, K^+, H^+) serve as the ion source. The introduced ions react with the electrodes and establish an open-circuit voltage, providing a clear electrical signal indicating the onset of sweat secretion.

The basic performance of the sensor for pressure sensing is presented in Figure 2b–d. In Figure 2b, as the forces applied to the sensor (radius: 5 mm) increase, the contact area between the electrode and the hydrogel increases, leading to a decrease in the contact resistance; thus, the output voltage decreases. The force is then converted into pressure. As shown in Figure 2c, it shows a linear relationship between pressure and output voltage, achieving a sensitivity of 1.58 mV kPa^{-1} in the range of 0–300 kPa and 0.66 mV kPa^{-1} in the range of 300–700 kPa. The measured pressure up to 700 kPa covers most plantar pressure values encountered during daily activities.[86] Meanwhile, durability and stability are crucial for ensuring reliable sensor performance under repeated mechanical loading. As shown in Figure 2d, the sensor is subjected to 24 hours (5000 cycles) of loading-unloading processes with an applied force of 30N, demonstrating excellent durability and stable output performance. Figure 2e–g illustrate the performance of the sensor for temperature sensing. Figure 2e demonstrates the voltage output response of the sensor under applied temperatures ranging from 30 to 50 °C, covering the typical human body temperature range. The output voltage remains stable at a constant value for each specific temperature, indicating good stability. Figure 2f presents the fitting results of voltage output versus temperature under applied pressures of 51, 115, and 191 kPa. The output voltage increases linearly with temperature under all three pressures. The fitted slopes show good consistency, which indicates that the temperature response is nearly independent of the applied pressure. Figure 2g presents the sensor response of hydrogel-based devices under 191 kPa with and without heating (Figure S5, Supporting Information). Due to the distinct working mechanisms of temperature and pressure sensing, these results demonstrate that the effects of temperature and pressure can be effectively decoupled, enabling reliable multimodal signal separation in subsequent analyses.[85] A temperature-pressure coupled response model across different pressures is established (Text S4, Supporting Information). This decoupling capability facilitates accurate multimodal sensing and calibration in practical scenarios.

Characterization results of the sweat sensor are shown in Figure 2h–j. As illustrated in Figure 2h, 5 µL of phosphate-buffered saline (PBS) solution, a commonly used artificial sweat simulant,[87] is dropped onto the hydrogel surface. The ions introduced by the PBS enabled the formation of an open-circuit voltage across the sensor, showcasing its potential for detecting the onset of sweat. In Figure 2i, the open-circuit voltage remains relatively constant as the volume of PBS increases. Since the open-circuit voltage is attributed to different redox properties of the top and bottom electrodes, the open-circuit voltage remains constant regardless of the ionic quantity. As shown in Figure 2j, the short-circuit current increased as PBS volumes increased. This is due to the increased amount of the introduced ions and the enhanced ion mobility within the hydrogel. Overall, the proposed hydrogel based on a single material is capable of multimodal sensing, including pressure, temperature, and sweat monitoring, and serves as a self-powered sensor for the further implementation of AEIS.

2.2. Advanced Yoga Evaluation Enabled by AI-Empowered Plantar Pressure Sensing

Leveraging the characteristics of self-powered sensing operation, high-pressure sensitivity, and intrinsic softness, we constructed the AEIS around this hydrogel platform. The integrated miniaturized PCB enables real-time acquisition and wireless transmission of 32-channel pressure signals. **Figure 3**a demonstrates the pressure response curves of the 32-channel hydrogel-based sensors during two cycles of spanning from forefoot contact through heel landing to full foot lift-off, highlighting the high sensitivity and stability of the smart insole for capturing dynamic pressure signals under various movements. To better visualize the plantar pressure distribution, pressure distribution heat maps are constructed. Each sensor is assigned a fixed spatial coordinate based on its physical layout within the insole. The 32-channel voltage signals are interpolated over a dense 2D mesh using a cubic interpolation algorithm for smooth visualization of pressure distribution across the plantar surface. The resulting data is rendered

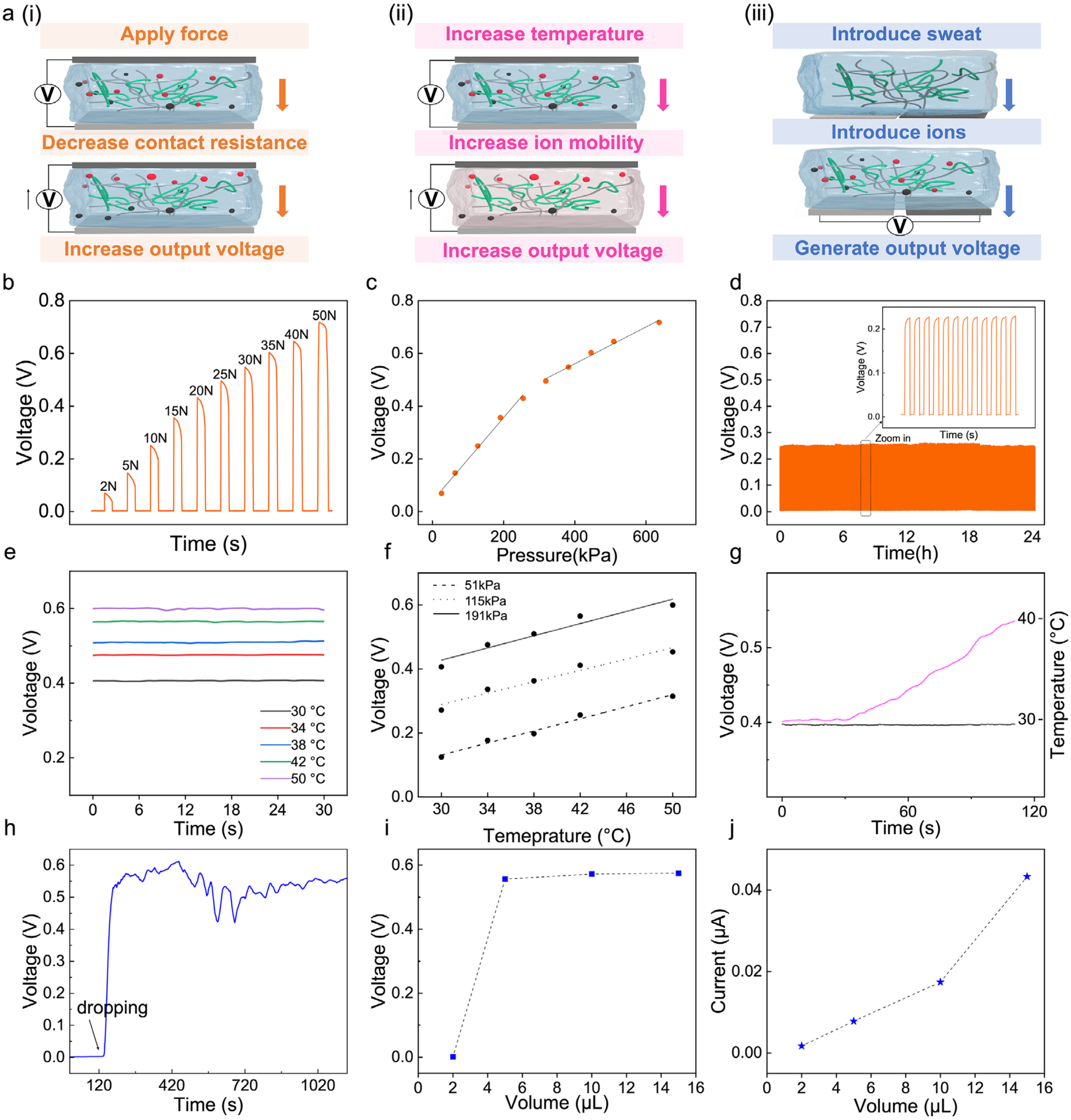

Figure 2. Multimodal self-powered sensing capabilities of the hydrogel-based sensors applied in the AEIS. a) Working principles and designation of multifunctional hydrogel sensor for detection of (i) pressure, (ii) temperature, and (iii) sweat. b) The output voltage under different forces and c) the corresponding output voltage under pressure. d) The output voltage changes under repeated loading-unloading processes with of 30N on the sensor for 24 hours (5000 cycles), showing the durability of the sensor. e) Voltage output curves of the sensor under different temperatures (at a constant pressure of 191 kPa), demonstrating stable response over 30 seconds. f) Experimental data and fitting results for voltage output over different temperatures under three different pressures. g) Response of hydrogel-based sensors under 191 kPa with (pink curve, 30–40 °C) and without heating (black curve). h) Generation of open circuit voltage when dropping PBS. i) Open circuit voltage output under different PBS volumes. j) Short circuit current output under different PBS volumes.

as heat maps, with color intensity representing the magnitude of applied pressure. Figure 3b shows the corresponding pressure distribution heat maps, from forefoot contact to heel landing. The high-density distributed sensor layout enables accurate spatial mapping across the plantar surface. Figure 3c illustrates dynamic pressure transitions from medial to lateral and from forefoot to heel, indicating precise tracking of pressure shifts across the foot during complex movements, which can be further used for gait pattern recognition and postural control analysis. In addition to dynamic monitoring, the hydrogel-based insole can

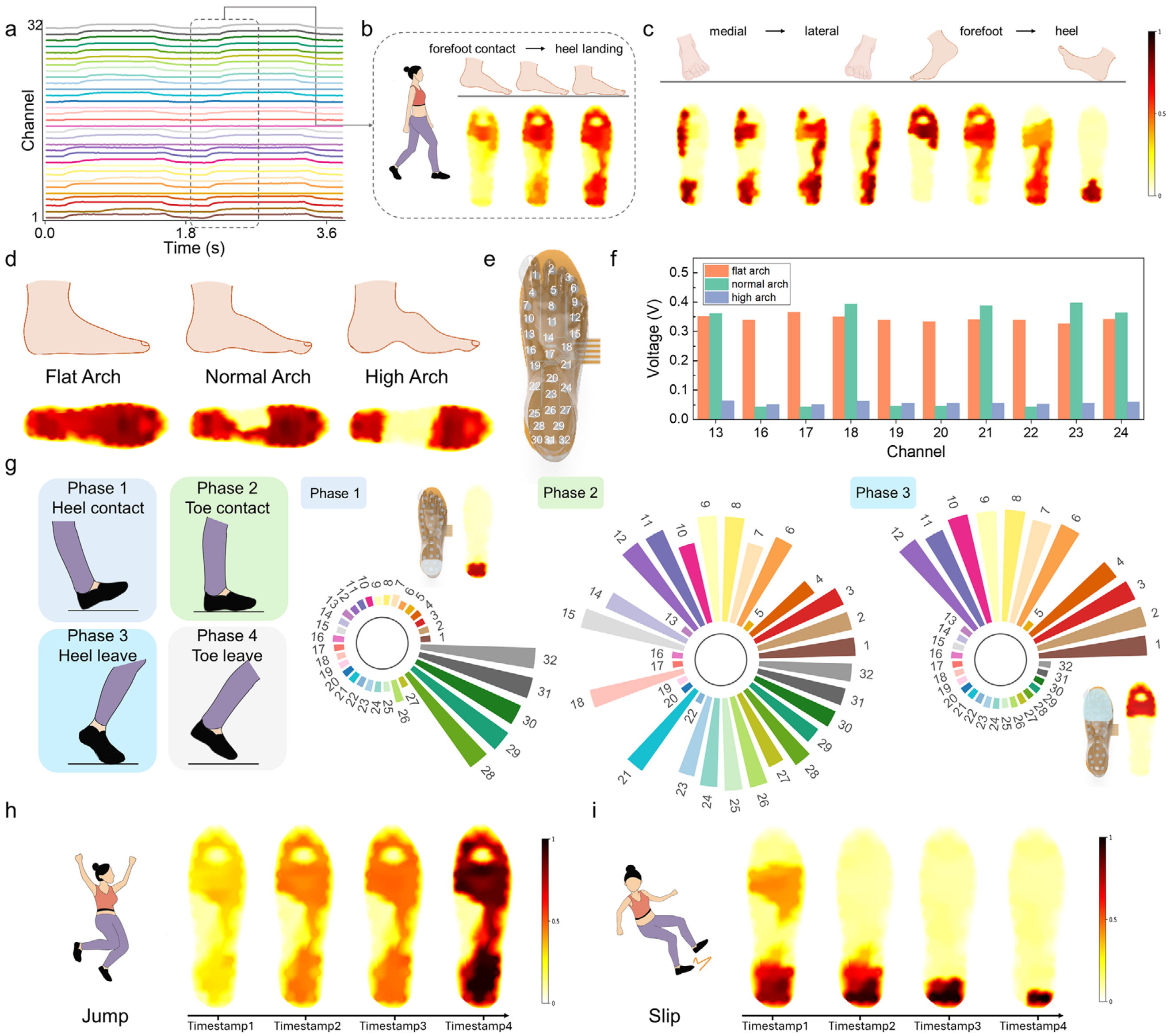

Figure 3. Design and characterization of smart insole for plantar pressure sensing. a) Pressure response curves of the 32-channel hydrogel-based sensors during two cycles of spanning from forefoot contact through heel landing to full foot lift-off, and b) the corresponding pressure distribution heat maps of half a cycle. c) Pressure distribution heat maps showing dynamic pressure shifts from medial to lateral and from forefoot to heel. d) Pressure distribution heat maps of three foot types: flat-arch foot, normal-arch foot, and high-arch foot. e) Configuration and distribution of the 32 sensors on the insole, sequentially labeled Channel 1 to 32 from the forefoot to the heel. f) Histogram of voltage responses of the channels located in the arch region for different foot types. g) Schematic illustration of the four phases of walking and the corresponding voltage responses at different stages: heel contact, toe contact, and heel leave. h) Dynamic pressure distribution heat maps of jumping, showing a gradual increase in pressure from initial ground contact to the peak loading moment. i) Dynamic pressure distribution heat maps during slipping, characterized by a rapid transition of load toward the heel and a gradual buildup of localized pressure.

characterize foot morphology, enabling static pressure mapping and identification of different arch types. As shown in Figure 3d, the pressure distribution heat maps of different foot types can be detected, including normal-arch foot, high-arch foot, and flat-arch foot. Due to variations in arch structure, the contact areas and pressure distributions differ significantly among the three types. Thus, the insole sensing system enables precise plantar pressure mapping, accurately capturing both dynamic and static pressure variations. The layout of the 32-channel sensor array is illustrated in Figure 3e, with sensor placement designed to provide comprehensive coverage of the plantar surface for accurate pressure mapping. The sensors positioned in the arch area enable a detailed assessment of midfoot loading characteristics. Figure 3f shows the voltage output recorded by the channels located in the arch area (Channel 13, 16–24) for different foot types. These results highlight the potential of our insole for foot type assessment and correction. Beyond static foot type characterization, the sequential distribution of sensors from the toe to the heel endows the smart insole with the capability to achieve dynamic gait monitoring by capturing the temporal feature of plantar pressure during walking.

Figure 3g demonstrates the variations in sensor signal amplitudes over a period of walking. The walking gait typically consists of four key phases: heel contact, toe contact, heel leave, and toe leave. The histogram of the 32-channel voltage outputs and the corresponding pressure distribution heat maps during three gait phases shows that pressure is sequentially transferred from the heel region (Channel 28–32) to the toe region (Channel 1–12). The real-time data acquisition and high temporal resolution of the self-powered insole allow clear segmentation of gait phases, highlighting the capability of the smart insole for advanced gait diagnostics. In addition to basic gait phase detection, the smart insole can also support activity monitoring, such as jumping and slipping. For example, Figure 3h visualizes the pressure distribution heat maps during jumping. Upon landing, the signal amplitudes gradually increase as the feet progressively contact the floor. Unlike walking, where ground contact occurs sequentially from the heel to the toe, jumping results in an almost simultaneous contact across the entire plantar surface. Figure 3i illustrates the dynamic pressure distribution heat maps during the process of slipping. The results show that pressure rapidly shifts toward the heel region, accompanied by a progressive concentration into a localized area. During slipping, the forefoot and midfoot regions gradually lose ground support, and the load becomes increasingly focused on the heel, eventually leading to complete loss of balance, and the slip occurs. The quick signal response and full-surface coverage of the smart insole support early detection of balance loss, making it suitable for fall risk monitoring and prevention. Overall, the smart insole achieves stable data acquisition without signal distortion. This confirms the effectiveness of the smart insole in accurate spatial and temporal monitoring of plantar pressure, enabling the reliable capture of static foot characteristics and dynamic gait events.

As yoga gains increasing popularity due to its physical, mental, and rehabilitative benefits,[88,89] the demand for effective yoga monitoring systems has become increasingly prominent. AEIS provides a reliable solution for real-time monitoring of plantar pressure during yoga without interfering with movement by integrating pressure sensors within footwear. Based on the collected pressure data, AI algorithms are capable of extracting relevant features and realizing yoga monitoring with high accuracy.[90–92] Our AEIS exhibits strong potential for monitoring plantar pressure during yoga practice due to its capabilities for both static and dynamic pressure sensing. Static plantar pressure profiles capture features of different yoga postures during yoga practice, while dynamic fluctuations provide crucial cues for detecting imbalance. By applying machine learning algorithms, AEIS can simultaneously realize yoga posture recognition and imbalance status detection for enabling a comprehensive evaluation during yoga practice. The workflow of AEIS is illustrated in **Figure** 4a, including a ResNet-18 model for the classification of 15 different yoga postures and a hybrid model selector (HMS) (Text S5, Supporting Information and Experimental Section) for the detection of three imbalance statuses: steady, slight imbalance, and moderate imbalance. First, the 32-channel plantar pressure data of 15 yoga postures are collected and transformed into spatial pressure distribution heat maps (Figure S6, Supporting Information). Then, they are subsequently fed into a ResNet-18 model to classify 15 different yoga postures (Experimental Section). Figure 4b demonstrates the pressure distribution heat maps of 15 yoga postures from a yoga practitioner, including Mountain Pose (Yoga1), Back Bend (Yoga2), Standing Side Stretch (Yoga3), Tree Pose (Yoga4), Standing Knee to Chest (Yoga5), Chair Pose (Yoga6), Chair Pose with Bound Hands Behind Variations (Yoga7), Standing Half Forward Bend (Yoga8), Half Forward Fold Hands on Floor (Yoga9), Standing Forward Bend Twist (Yoga10), Garland Pose (Yoga11), High Lunge (Yoga12), High Lunge with Arms Extended Forward (Yoga13), High Lunge Pose Backbend (Yoga14), and Standing Forward Fold (Yoga15). These yoga postures are categorized as double-leg standing (Yoga1), side/back bending (Yoga2, Yoga3), single-leg balancing (Yoga4, Yoga5), double-leg squatting (Yoga6, Yoga7, Yoga11), forward bending (Yoga8-10, Yoga15), and lunge-based postures (Yoga12-14). Compared to double-leg standing (Yoga1), the pressure distribution heat map of Yoga3 shows slightly greater loading on the medial forefoot (near the big toe), compared to the lateral side (near the little toe), possibly due to a lateral shift of the center of gravity and associated inward rotation of the supporting foot. Yoga2 exhibits a similar plantar pressure distribution to Yoga1, with minor differences. Single-leg postures (Yoga4, Yoga5) exhibited significantly higher pressure on the supporting foot, as it bears the entire body weight to maintain balance. In double-leg squatting postures (Yoga6, Yoga7, Yoga11), a noticeable increase in forefoot pressure is recorded, possibly due to a forward displacement of the center of gravity. Similarly, forward-bending postures (Yoga8-10, Yoga15) also demonstrate higher plantar pressure in the forefoot. A distinct medial bias in heel pressure is observed in Yoga10, in contrast to Yoga8 and Yoga9, which may be associated with internal foot rotation in response to the trunk twist. In comparison, Yoga15 presents a continuous pressure band along the metatarsophalangeal groove, likely resulting from deeper upper-body flexion and a more pronounced anterior weight shift. In lunge-based postures (Yoga12-14), the rear heel typically does not contact the ground, resulting in no pressure distribution in that region. Pressure distribution heat map of Yoga12 shows greater pressure concentration on the lateral forefoot, while in Yoga 13, pressure shifts toward the medial forefoot, with a notable concentration near the big toe. For Yoga14, the force-bearing area of the forefoot expands, likely associated with the need to maintain balance during backward leaning.

Building on the observed differences in pressure distribution patterns, the ResNet-18 model is employed to extract spatial features from the heat maps and achieved 98.33% classification accuracy across the fifteen yoga postures (Figure 4c). A one-dimensional convolutional nerual network (1D-CNN) model is leveraged to investigate the impact of sensor channel density and spatial placement on classification performance. According to the established foot partitioning schemes (Figure S7, Supporting Information),[59] we incrementally deploy sensors and evaluate classification accuracy across configurations ranging from 4 to 32 channels (Figure 4d). In the 4-channel configuration, sensors are positioned at the heel, lateral midfoot, medial forefoot, and hallux, which are represented as dark gray circles in the layout. As a result, the 4-channel configuration achieves an average classification accuracy of 68.13% over 10 repetitions. Compared to the 4-channel setup, the 8-channel configuration increases

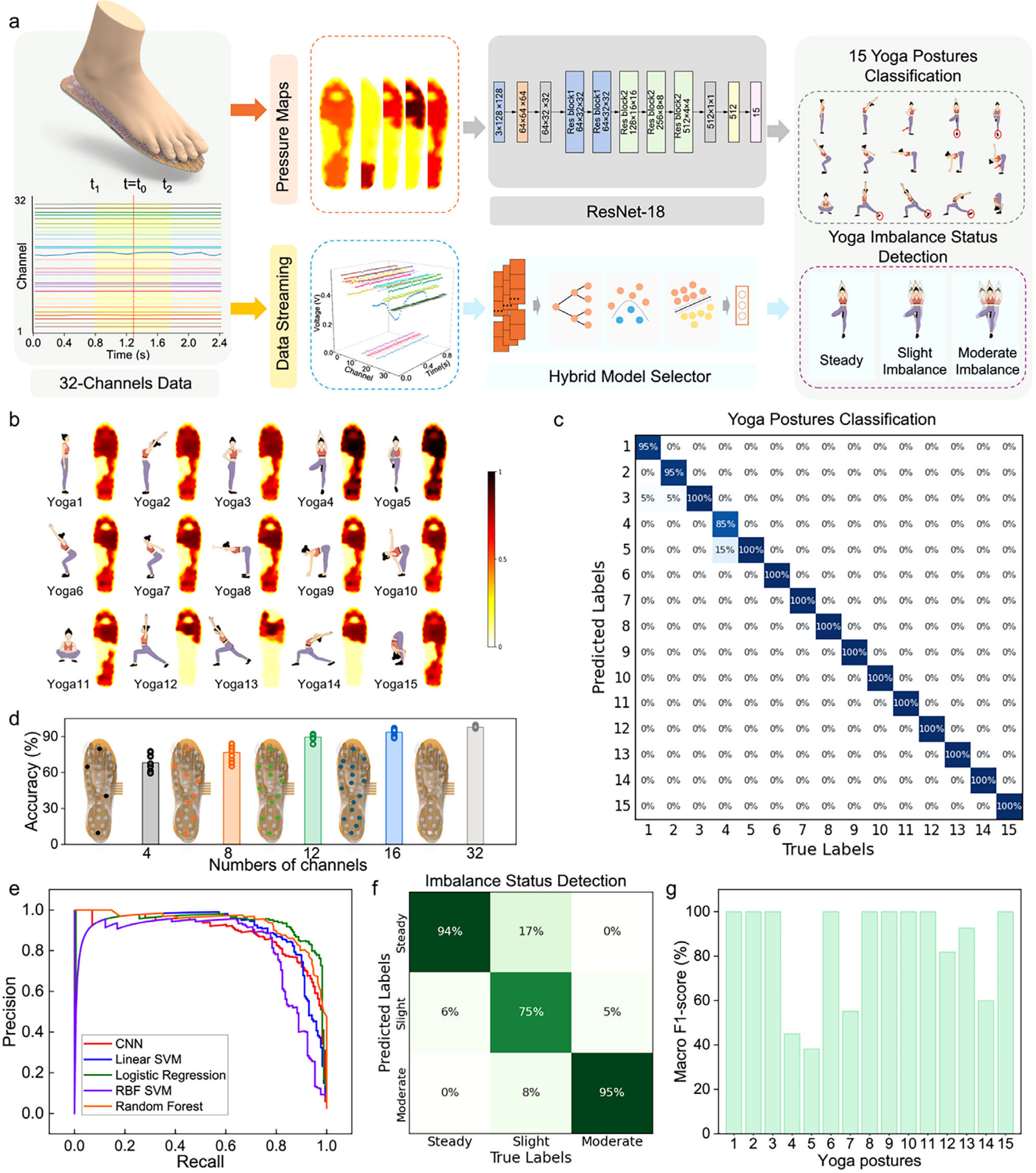

Figure 4. AI-Empowered Evaluation Framework for Yoga Posture Classification and Imbalance Detection. a) Workflow of yoga posture classification using ResNet-18 and imbalance detection based on a HMS. b) Pressure distribution heat maps of 15 different yoga postures, including: Mountain Pose (Yoga1), Back Bend (Yoga2), Standing Side Stretch (Yoga3), Tree Pose (Yoga4), Standing Knee to Chest (Yoga5), Chair Pose (Yoga6), Chair Pose with Bound Hands Behind Variations (Yoga7), Standing Half Forward Bend (Yoga8), Half Forward Fold Hands on Floor (Yoga9), Standing Forward Bend Twist (Yoga10), Garland Pose (Yoga11), High Lunge (Yoga12), High Lunge with Arms Extended Forward (Yoga13), High Lunge Pose Backbend Yoga14), and Standing Forward Fold (Yoga15). c) Confusion map of the classification of 15 yoga postures. d) Classification accuracy of yoga postures with varying numbers of smart insole channels (4, 8, 12, 16, and 32 channels). Bars represent the average accuracy over 10 trials, and the dots on the bars indicate the corresponding results from individual runs. The corresponding configurations are shown on the left side of the bars. e) Precision-recall curves of different ML models for imbalance status detection. f) Confusion map of imbalance status detection via soft voting strategy. g) The yoga posture classification accuracy based on macro-averaged F1-score for each yoga posture.

sensor density at the heel and introduces sensors in new regions, including the central and lateral forefoot. This configuration is represented as circles in orange, yielding a modest improvement in average accuracy to 76.67%. The 12-channel configuration (green circles) enhances spatial resolution by increasing sensor coverage in the heel, medial midfoot, central forefoot, and toe regions. In this configuration, all regions defined in the foot partitioning scheme are covered by at least one sensor, and the average classification accuracy improved to 89.4%. With a 16-channel configuration (blue circles), increased sensor density in the heel, mid-foot, central foot, and hallux improves the average accuracy to 93.6%. Finally, the full 32-channel configuration provides dense coverage across the entire plantar surface, resulting in a significant improvement in classification accuracy to 97.8%. The confusion maps and macro F1-score of 15 yoga postures in different configurations are shown in Figure S8 (Supporting Information). The classification accuracy of the 15 yoga postures increases with the number of sensing channels.

To detect imbalance status during yoga practice, 32-channel temporal sequences are segmented using a 50-point sliding window with a step size of 10. The resulting segments are then fed into the HMS to classify three imbalance statuses: steady, slight imbalance, and moderate imbalance. The HMS integrates predictions from five candidate models using a soft voting strategy, including a 1D-CNN, random forest (RF), linear support vector machine (SVM), radial basis function (RBF) SVM, and logistic regression (LR). The precision-recall curves of these individual models are shown in Figure 4e, and their confusion maps are presented in Figure S9 (Supporting Information). The classification performance using soft voting strategy is shown in Figure 4f,g, achieving an accuracy of 90.06%. The proposed HMS enables a robust and adaptive strategy for imbalance status detection by leveraging the strengths of multiple classifiers. Compared to conventional insole systems, our AEIS enables advanced plantar pressure sensing through the integration of a multi-channel hydrogel-based insole and AI data analytics for yoga evaluation. The self-powered hydrogel, with high pressure sensitivity, can detect both static foot characteristics and dynamic gait events. The collected data is wirelessly transmitted to the AI-enabled cloud server for yoga posture recognition (Video S1, Supporting Information) and imbalance state detection (Video S2, Supporting Information).

2.3. Advanced Yoga Evaluation Enabled by AI-Empowered Plantar Pressure Sensing

Accurate posture assessment is essential for improving performance and preventing injury, particularly among beginners. Passive assessments, such as yoga posture recognition and imbalance status detection, can only inform practitioners about their current performance but do not provide insights to facilitate self-improvement. Effective yoga practice requires both center-of-gravity control and postural stability, highlighting the need for an intelligent coaching system capable of delivering targeted guidance. By collecting plantar pressure data from a professional yoga coach to train AI models, an intelligent yoga coaching system can be developed to offer personalized guidance for yoga practitioners. An 1D CNN model is developed for multi-user recognition (**Figure** 5a), which comprises three convolutional layers, two adaptive average pooling layers, and two fully connected layers that outputs the predicted identity of four users (User 1: male, 30 years old, Yoga coach, 10-year yoga practice; User 2: female, 45 years old, 2-year yoga practice; User 3: female, 26 years old, 3-month yoga practice, User 4: female, 55 years old, 3-year yoga practice). The model achieves a user identification accuracy of 100% (Figure 5b) for 6 yoga postures. Six representative postures are selected due to their distinct challenges to stability, including double-leg standing (Yoga1), single-leg balancing (Yoga4), double-leg squatting (Yoga6, Yoga11), lunge-based postures (Yoga12), and forward bending (Yoga15). These postures span a range of stability demands, from simple bilateral standing to more complex single-leg and asymmetrical weight-bearing positions. Once the user is recognized, the system compares their COP stability parameters with the predicted expert-like values to generate personalized guidance. To better analyze the plantar pressure distribution of the yoga coach and practitioners, the foot is segmented into six regions with the corresponding ratios (Text S6, Supporting Information): forefoot (r_f), arch (r_a), heel (r_h), left (r_l), center (r_c), and right (r_r). Figure 5c presents six plantar pressure distribution ratios of different users during the practice of Yoga 11. Plantar pressure distribution ratios of other postures are shown in Figure S10 (Supporting Information). Compared with User 1 (Yoga coach), User 3 and User 4 exhibit higher forefoot pressure ratios, suggesting a weight shift toward the front. User 2 displays a similar forefoot-arch-heel distribution to User 1 but shows a lower pressure ratio on the right side, indicating a tendency to lean to the left. Then, we want to explore the stability performance of the yoga practitioners and provide personalized guidance to improve their postural stability. To this end, six regional ratios are used as the input features of the RF regressor-based pipeline (Figure 5d). Pressure distribution heat maps of the four different users are visualized using distinct colors: User 1 (Yoga coach) in pink, User 2 in blue, User 3 in orange, and User 4 in green. Pressure distribution heat maps of the other yoga postures are shown in Figure S11 (Supporting Information). COP, a key indicator of postural control, plays a critical role in assessing stability during yoga postures. It is computed at each time point based on signals from the 32-channel sensor array[93,94] and is defined as

$$x_i = \frac{\Sigma_{j=1}^{n} P_j^{(i)} * x_j}{\Sigma_{j=1}^{n} P_j^{(i)}} \tag{1}$$

$$y_i = \frac{\Sigma_{j=1}^{n} P_j^{(i)} * y_j}{\Sigma_{j=1}^{n} P_j^{(i)}} \tag{2}$$

where x_i and y_i represent the anterior-posterior and medial-lateral components of the COP at the time step i, respectively. n represents the number of sensors (Channel 1–32), $P_j^{(i)}$ represents the pressure value measured by the sensor j at the time step i, and x_j and y_j represent the coordinates of the sensor j on the insole.

Four COP-based stability parameters are extracted from the COP time-series data to assess the practitioners' postural stability during yoga practice. These parameters include root mean square distance (D_{RMS}), total path length (TPL), ellipse area (EA), and

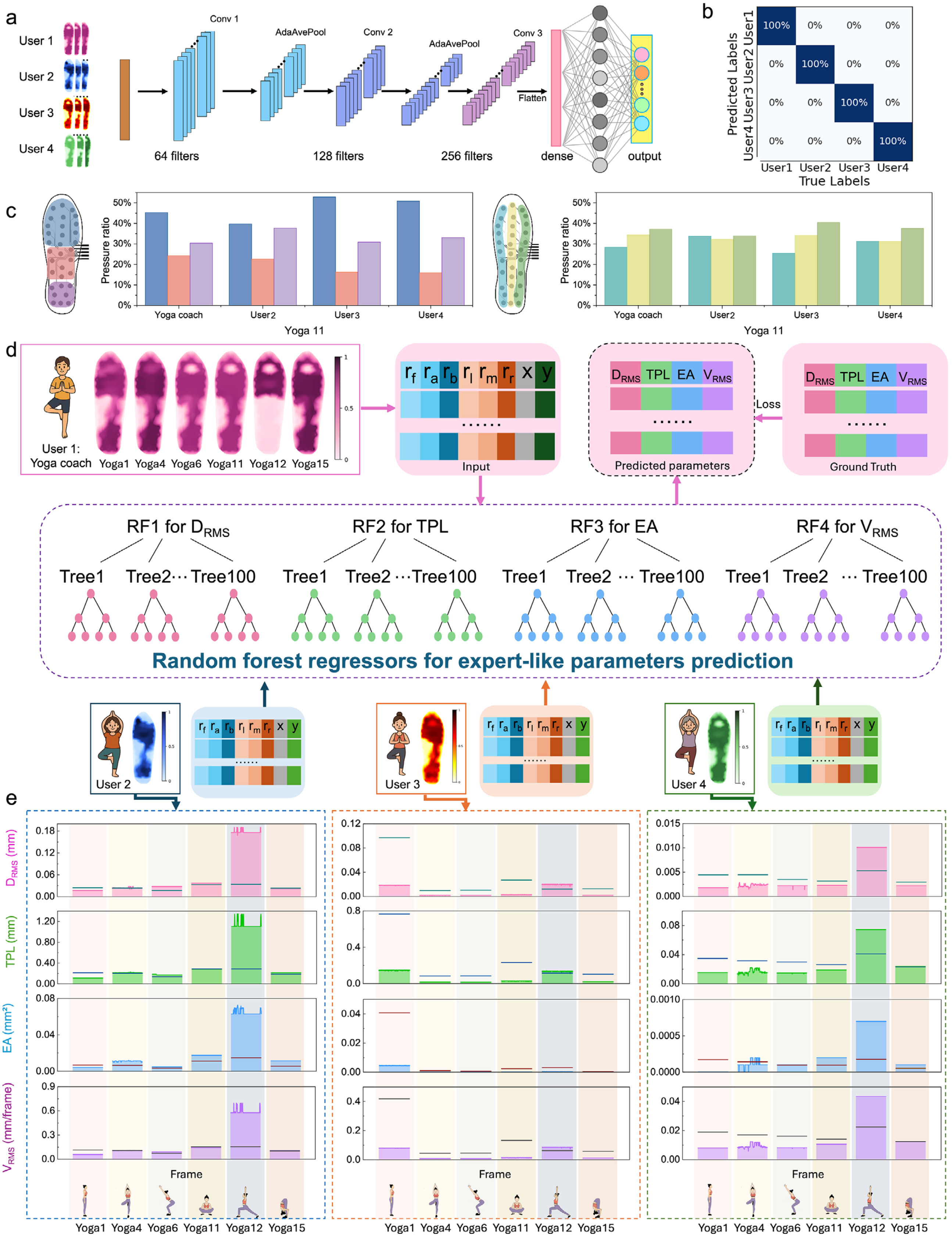
a
User 1
User 2
User 3
User 4
Conv 1
AdaAvePool
Conv 2
AdaAvePool
Conv 3
Flatten
64 filters
128 filters
256 filters
dense
output
b
Predicted Labels
User4 User3 User2 User1
100% 0% 0% 0%
0% 100% 0% 0%
0% 0% 100% 0%
0% 0% 0% 100%
User1 User2 User3 User4
True Labels
c
Pressure ratio
50%
40%
30%
20%
10%
0%
Yoga coach
User2
User3
User4
Yoga 11
d
User 1:
Yoga coach
Yoga1 Yoga4 Yoga6 Yoga11 Yoga12 Yoga15
1
0.5
0
r_f r_a r_b r_l r_m r_r x y
Input
D_{RMS} TPL EA V_{RMS}
Predicted parameters
Loss
Ground Truth
RF1 for D_{RMS}
RF2 for TPL
RF3 for EA
RF4 for V_{RMS}
Tree1 Tree2 ··· Tree100
Random forest regressors for expert-like parameters prediction
User 2
User 3
User 4
e
D_{RMS} (mm)
TPL (mm)
EA (mm²)
V_{RMS} (mm/frame)
0.18
0.12
0.06
0.00
1.20
0.80
0.40
0.9
0.6
0.3
0.0
0.12
0.08
0.04
0.8
0.4
0.02
0.2
0.015
0.010
0.005
0.000
0.0010
0.0005
0.0000
Frame
Yoga1 Yoga4 Yoga6 Yoga11 Yoga12 Yoga15

root mean square velocity (V_{RMS}).[95] D_{RMS} quantifies the root-mean-square displacement of the COP from its mean position, TPL represents the total path length of the COP trajectory, EA denotes the area of the covariance ellipse constructed from the COP trajectory, and V_{RMS} measures the root-mean-square velocity of COP movement. The extracted COP-based stability parameters enable us to analyze and compare COP shifts, reflecting the varying levels of skill, control, and stability between practitioners and the yoga coach. These parameters form a comprehensive representation of stability control during yoga practice, which can be defined as:

$$D_{RMS} = \sqrt{\frac{1}{N-1}\sum_{i=1}^{N}\left(\left(x_i-\bar{x}\right)^2+\left(y_i-\bar{y}\right)^2\right)} \tag{3}$$

$$TPL = \sum_{i=1}^{N-1}\sqrt{\left(x_{i+1}-x_i\right)^2+\left(y_{i+1}-y_i\right)^2} \tag{4}$$

$$V_{RMS} = \sqrt{\frac{1}{N-1}\sum_{i=1}^{N-1}\left(\frac{\left(x_{i+1}-x_i\right)^2+\left(y_{i+1}-y_i\right)^2}{\Delta t^2}\right)} \tag{5}$$

where N is the number of time points in the COP trajectory, $(\bar{x}, \bar{y})$ is the mean of the current COP coordinate (x_i, y_i) and COP coordinates of the two preceding frames, Δt denotes the interval between adjacent frames.

$$EA = 2\pi \cdot \sqrt{\left|\lambda_1 \cdot \lambda_2\right|} \tag{6}$$

where λ_1, $\lambda_2$are the eigenvalues of the covariance matrix C constructed from the COP coordinates (x_i, y_i) over time. The matrix C is given by:

$$C = \begin{bmatrix}\sigma_{xx}\sigma_{xy}\\ \sigma_{xy}\sigma_{yy}\end{bmatrix} \tag{7}$$

with:

$$\begin{cases}\sigma_{xx} = \frac{1}{N-1}\sum_{i=1}^{N}\left(x_i-\bar{x}\right)^2\\ \sigma_{yy} = \frac{1}{N-1}\sum_{i=1}^{N}\left(y_i-\bar{y}\right)^2\\ \sigma_{xy} = \frac{1}{N-1}\sum_{i=1}^{N}\left(x_i-\bar{x}\right)\left(y_i-\bar{y}\right)\end{cases} \tag{8}$$

A RF-based regression pipeline is developed using plantar pressure signals derived from User 1 (Yoga coach) as expert references (Figure S12, Supporting Information) to provide personalized feedback for postural stability. For each user and posture, plantar pressure signals are recorded across 200 consecutive time frames to capture the temporal dynamics of pressure distribution. The model is composed of four separate random forest regressors (each consisting of 100 decision trees), trained to predict four COP-based stability parameters: D_{RMS}, TPL, EA, and V_{RMS}. The inputs of the model include the COP coordinates (x, y) and 6 pressure ratios $(r_f, r_a, r_h, r_l, r_c, r_r)$. Once trained, the model takes the plantar pressure signals of a practitioner and generates expert-like predictions of COP stability parameters, representing the expected values if the posture is performed with expert-like control. These predicted parameters serve as personalized targets to guide users toward improved postural stability. As a result, as shown in Figure 5e, the predicted master style reference ranges for the four COP-based stability parameters D_{RMS}, TPL, EA, V_{RMS} are shown as shaded areas in pink, green, blue, and purple, respectively. The solid curves represent the corresponding values computed directly from the COP coordinates of the three practitioners. The yoga coaching system provides expert-like personalized feedback based on whether the measured values of the practitioners fall within the predicted master style reference ranges. When the parameter curve lies within the corresponding shaded region, the performance is assessed as good. For example, all the measured parameters of User 2 during the practice of Yoga12 fall within the predicted range, indicating that User 2 performed Yoga12 with good stability and control. Otherwise, the system generates targeted suggestions based on the deviation of different parameters. For the same posture, the measured EA of User 3 during Yoga12 falls outside the predicted range, indicating that User 3 needs to better control the sway area and focus on balance training to reduce instability. In the case of User 4, the measured D_{RMS} exceed the predicted thresholds, suggesting a need to enhance core control and keep the center of gravity concentrated. TPL is also beyond the expected range, which indicates that User 4 needs to reduce movement adjustments and practice static poses. Additionally, the V_{RMS} surpasses the acceptable predicted threshold, indicating that User 4 is in frequent shaking and needs to consider pairing with breathing exercises to reduce pace. By leveraging the AI-enabled yoga coaching system, practitioners can receive real-time expert guidance tailored to their performance of yoga practice. Such intelligent guidance facilitates standardized posture execution and accelerates the learning process, especially for beginners lacking in-person instruction.

Building on the expert-like stability guidance provided by the RF regression model, we further integrated a haptic feedback array and a Unity-based VR environment to address the limitation of verbal-only instructions, which often fail to help users accurately perceive and correct their postural inaccuracies. In the virtual environment, the digital twin of the user provides a more intuitive visual representation based on real-time sensor outputs, allowing for better detection of the motion status of the user. In parallel, a yoga coach avatar is displayed to offer posture guidance. The integration of haptic feedback allows users to physically sense the incorrect pressure distribution. This approach enables

Figure 5. AEIS-Enabled Yoga Coaching System for Guiding Multiple Users in Training. a) Schematic of the process and key parameters for building the 1D CNN architecture for user recognition. b) Confusion map of user recognition. c) Comparison of foot pressure distribution ratios across key foot regions (forefoot, arch, heel, left, center, right) during six yoga postures between a yoga master and three users. d) Schematics of the ML framework for the yoga coaching system. RF regressors are trained using COP and foot pressure ratios to predict four COP-based stability parameters (D_{RMS}, TPL, EA, V_{RMS}), enabling personalized feedback. e) Comparison of the four real stability parameters of three users with the ML-predicted master style parameters across six yoga postures. For each parameter, the shaded area below the threshold indicates good performance in line with the master style, while values above the shaded area indicate deviations requiring improvement suggestions. Pink, green, blue, and purple shaded areas represent D_{RMS}, TPL, EA, V_{RMS}, respectively.

AEIS to significantly improve the immersive experience and the effectiveness of yoga training. As shown in **Figure** 6a, the proposed metaverse-enabled yoga coaching system integrates multimodal physiological monitoring, haptic stimulation, and real-time VR/AR visualization, forming a closed-loop, user-centered immersive yoga training framework. Sensor signals from the 32 channels are collected using multiplexers (MUXs) and processed by a microcontroller unit (MCU) embedded within the insole (Figure 6a(i)). Based on the multifunctional hydrogel sensors and a miniaturized, custom-designed miniaturized PCB, the system enables simultaneous pressure sensing, temperature monitoring, and sweat detection. The processed multimodal data is wirelessly transmitted to the terminal via a Bluetooth module. These multimodal signals allow not only for postural guidance but also for real-time physiological monitoring, providing insights into physical exertion and enabling a more comprehensive monitoring of the user's health status. Among 32 hydrogel-based sensors, 30 sensors distributed across a 32-channel array are used for pressure sensing, along with a temperature sensor and a sweat sensor (Figure 6a(ii)). A sweat sensor and a temperature sensor are placed into channel 9 (blue) and channel 12 (pink), respectively, while channel 15 (yellow) serves as a reference pressure sensor to decouple pressure-related contributions from the temperature signal. All three sensors are located in the lateral forefoot region. By applying a two-step decoupling approach based on the voltage output of the sensors, temperature information is successfully decoupled. The observed output potential from the sweat sensor confirms successful sweat detection. As shown in Figure 6(iii), during the initial 10 seconds after the start of exercise, the voltage output of the sweat sensor remained at 0 V due to the absence of ion introduction resulting from sweat production. The output from the temperature sensor closely matched that of the pressure reference channel, implying that no significant temperature change had occurred at this stage. After 120 seconds, the sweat sensor output remained at 0 V, indicating continued absence of ions, while the voltage output of the temperature sensor began higher than the pressure reference channel. This deviation suggests a temperature rise, estimated at ≈33 °C based on the calibration curve. After 1800 seconds of continuous yoga practice, the sweat sensor exhibited a noticeable voltage output due to ion introduction from sweat production, while the temperature sensor simultaneously showed an additional voltage rise corresponding to a cumulative temperature increase of ≈1 °C based on the calibration curve.

In addition to the multimodal sensing system, our AEIS systems integrate a haptic feedback array including four low-power eccentric rotating mass vibrators embedded at the front (blue), back (green), left (gray), and right (red) regions of the insole to enhance the effectiveness of yoga training and provide a direct sense of incorrect posture. The calibration curve between vibration amplitude and voltage is relatively linear (Figures S13 and S14, Supporting Information), enabling adjustable vibration intensity through voltage control. Then we utilize these localized vibrations to deliver real-time feedback regarding plantar pressure ratio (PPR) shifts (Figure 6a(iv)). The PPR is defined as the ratio of pressure outputs between the front (r_{front}) -back (r_{back}) and left (r_{left}) -right (r_{right}) foot regions (Text S7, Supporting Information). We compared the PPR of users with the PPR of the yoga coach, which are then mapped to corresponding vibrators to remind the users of their improper posture. For example, haptic alerts for User 2 during yoga6 and User 3 during yoga11 are demonstrated in Figure 6b. For the case shown in Figure 6b(i), at timestamp1 and timestamp2, the forefoot PPR (r_{front}) of User 2 exceeds the threshold2, while the right plantar PPR (r_{right}) exceeds the threshold1. As a result, the AEIS activates the front unit (C_f) to deliver a moderate vibration feedback and the right unit (C_r) to provide light feedback. At timestamp 3, when all PPRs of the user fall below threshold 1, the vibration feedback is accordingly deactivated. Similarly, for User 3 (Figure 6b(ii)), strong haptic feedback is delivered to the forefoot and light feedback to the left side, suggesting a forward and leftward shift in pressure distribution that deviates from the PPR of the yoga coach.

To enhance immersive interaction, a metaverse-enabled yoga coach avatar is established in the virtual space (see Figure S15, Supporting Information and Experimental Section). The working flowchart is shown in Figure 6a(v). The digital-twin-based system first recognizes the current yoga posture, then continuously monitors the PPR shifts and predicts expert-like COP-based parameters by the AI-enhanced system. When a PPR shift is detected, directional haptic feedback is triggered to guide posture correction. Meanwhile, the personalized suggestions for yoga practice will be generated based on the predicted expert-like COP-based parameters. Overall, the proposed AEIS integrates pressure, temperature, and sweat sensing with haptic feedback to support both physiological monitoring and posture correction throughout the yoga training process. By enabling real-time assessment and feedback, a metaverse-enabled yoga coach avatar can provide personalized guidance and corrective feedback for an immersive VR-based yoga training experience (Video S3, Supporting Information).

3. Conclusion

We have developed an AEIS that integrates multifunctional hydrogel with self-powered pressure, temperature, and sweat sensing capabilities to collect comprehensive plantar information, along with haptic units, a metaverse-based yoga coach, and a digital twin of the user for more immersive VR yoga training. This system features an optimized 32-channel signal array, wirelessly transmitted via a customized miniaturized circuit embedded in the insole for subsequent AI-based analysis. The AEIS also converts the signals into heat maps, offering detailed insights into plantar pressure distributions. Building on these capabilities, AEIS integrates machine learning algorithms to classify 15 yoga postures based on the pressure distribution heat maps, achieving an accuracy of 98.33%. Additionally, imbalance status detection based on sequential data is achieved with an accuracy of 90.06%. Leveraging advanced AI data analytics, a virtual yoga coaching system is proposed, capable of recognizing different users and providing personalized guidance. The proposed RF regression model is trained by the expert yoga instructor to learn the mapping between pressure signals and corresponding stability parameters. Then the model predicts the expected expert-level stability parameters for that posture according to users' input, guiding users toward improved stability and control that resemble expert performance. By utilizing the PPR shifts to trigger the integrated vibrators, adjustable vibro-haptic feedback is achieved to correct the users' yoga posture. Furthermore, AEIS integrates

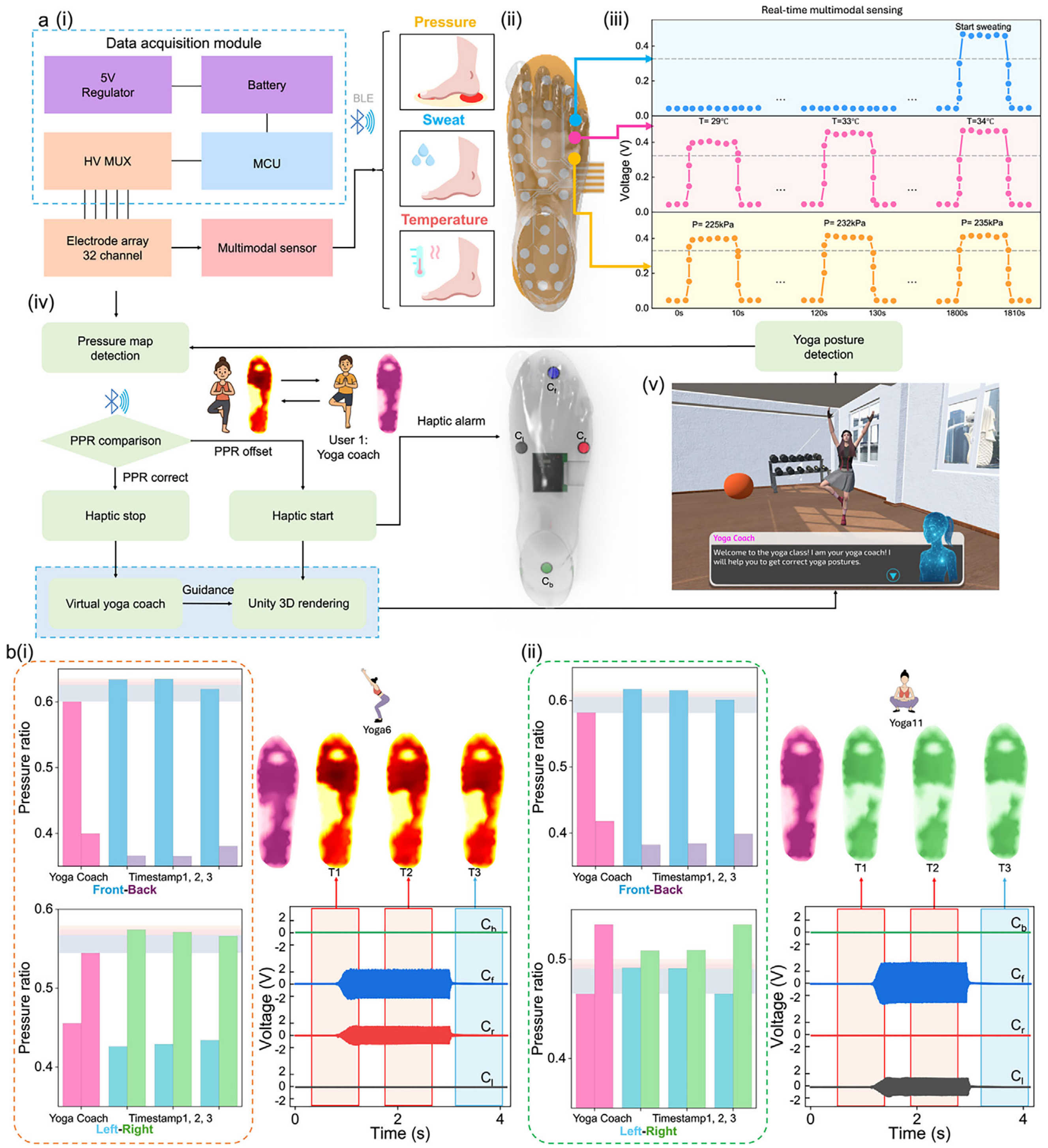

Figure 6. AEIS for Real-Time Multifunctional Sensing and Immersive Metaverse-Based Yoga Training. a) Workflow diagram of the digital-twin based yoga coaching system. (i) Schematic of data acquisition module (ii) Schematic of the 32-channel multifunctional insole sensor array, comprising 30 pressure sensors, 1 temperature sensor, and 1 sweat sensor. (iii) Real-time multifunctional sensing of pressure, temperature, and sweat during exercise. (iv) Four haptic units are distributed to deliver directional haptic feedback corresponding to PPR shifts toward the left (gray), right (red), front (blue), or back (green). (v) A metaverse-enabled yoga coach avatar is built in virtual space, providing real-time posture correction and personalized guidance based on user performance for digital twin-based dynamic interaction. b) Demonstration of haptic alerts for (i) User 2 when practicing Yoga6 and (ii) User 3 when practicing Yoga11. Three thresholds are set to compare users' PPR with the PPR of the Yoga coach. When deviations exceed these thresholds, the system activates corresponding vibrators at three distinct intensity levels to alert users of improper posture.

an interactive metaverse platform that provides users with cross-space perception capability. The virtual yoga coach provides real-time, remote guidance and posture correction through simulated stimuli and feedback for training users. This breakthrough offers users an immersive, face-to-face-like virtual yoga-coach-guiding experience. The development of the metaverse infrastructure will promote the construction of sports training centers in the virtual world. Empowered by immersive VR, multimodal sensory technologies, and real-time feedback, the metaverse-enabled yoga coach will deliver personalized guidance and real-time correction, supporting a wide range of training scenarios, including fitness, rehabilitation,[96–98] and immersive learning.

4. Experimental Section

Fabrication of Hydrogel-Based Self-Powered Sensor for Multimodal Sensing: The hydrogel is synthesized through the following steps. First, 15.0128 g of Poly(vinyl alcohol) polymers (PVA, Mw 89 000–98 000, 99+%, hydrolyzed, 341584), 0.39052 g of lithium chloride powder (LiCl, ACS reagent, ≥99%, 310468), and 0.675576 g of glycerin (Gly, for molecular biology, ≥99.0%, G5516) are pre-mixed in 90 mL of deionized (DI) water at room temperature. (Note: for sweat sensing, LiCl is omitted from this step to avoid introducing ionic conductivity.) The resulting solution is then transferred to a 90 °C water bath and stirred at 400 rpm for 90 minutes to ensure complete dissolution. After cooling the mixture to room temperature, 0.01 g of N, N'-Methylenebisacrylamide (MBA, powder, for molecular biology, suitable for electrophoresis, ≥99.5%, M7279), 0.03 g of ammonium persulfate (APS, for molecular biology, suitable for electrophoresis, ≥98%, A3678), and 7.5064 g of acrylamide monomers (AAm, for molecular biology, ≥99% (HPLC), A9099) are added. The solution is then stirred at 400 rpm in a 40 °C water bath for 30 minutes to ensure full dissolution. After cooling to room temperature and removing entrapped air bubbles, the precursor solution is poured into customized 3D-printed molds made of PLA (PolyLite, Polymaker). The samples are first dried in a dry cabinet at 20% relative humidity and 24 °C for 24 hours, followed by an additional 48 hours of drying in an environmental chamber at 60% RH and 24 °C. After the drying process, the PVA/PAAm/LiCl/Gly hydrogels are carefully demolded. The PVA/PAAm/Gly/LiCl insole-shaped hydrogel layer is then applied for pressure sensing (Figure S2, Supporting Information). The hydrogel layer is attached to the 32-channel silver electrode array using a laser-cut piece of double-sided adhesive film (3M VHB Tape), which matched the insole outline and included cutouts to expose the underlying electrode patterns. An additional adhesive film, identical in shape and cutouts, is applied on top of the hydrogel to enable integration of the upper aluminum electrode layer (aluminum foil tape, 1436, 3M) (Figure S3, Supporting Information). To incorporate temperature and sweat sensing into the multimodal system, two regions of the insole-shaped hydrogel layer, originally applied for pressure sensing, are cut out to expose the underlying electrodes (Figure 6a(ii)). A 2 cm × 2 cm PVA/PAAm/Gly/LiCl hydrogel patch is then applied for temperature sensing. For sweat sensing, a 2 cm × 2 cm hydrogel patch without LiCl is placed across the silver and aluminum electrodes (Figure 2a(iii)), with its upper surface left exposed to allow direct sweat absorption, thereby enabling ionic conduction only when sweat is present. The calibrations of output voltage against force for the hydrogel-based pressure sensor are conducted by force gauge (Mecmesin, MultiTest 2.5-i).

Hydrogel-Based Sensor Characterization: The potential outputs in the characterization of the hydrogel-based pressure, temperature, and sweat sensor are measured by an oscilloscope (Agilent, DSO-X3034A) using a normal probe of 1 Mohm impedance. The current output of the hydrogel-based sweat sensor is measured by an electrometer (Keithley, 6514), and the signals are displayed and recorded by the oscilloscope.

System Design of Data Collection: A customized PCB is designed for voltage collection during IoT applications (an illustration of circuit design is shown in Figure S4, Supporting Information). It is controlled by a MCU (Mega2560 Pro) with 16 analog-to-digital converter (ADC) channels. Four 8-to-1MUXs (74HC4051) are employed to expand input capacity to 32 channels. Each MUX is controlled by three selection lines to determine the active input channel. LM324 operational amplifiers are used for signal enhancement. A Bluetooth module (CC2530) is also integrated for wireless data transmission. After signal acquisition and wireless transmission, the 32 collected pressure values are assigned to their corresponding spatial regions for further analysis.

Machine Learning Development: For yoga posture classification, the pressure distribution heat maps are fed into a RestNet-18 model. The model architecture is illustrated in Figure 4a. Training is conducted for 5 epochs using Cross Entropy Loss as the loss function and the Adam optimizer (learning rate = 0.001), with a training-to-testing split ratio of 9:1. To compare the classification accuracy performance under different numbers of sensing channels, the raw pressure data are normalized, and the selected channel data are directly used as input for a 1D-CNN. The 1D-CNN model consists of three convolutional layers with 64, 128, and 256 filters (kernel size = 3, padding = 1), each followed by ReLU activations. Adaptive average pooling is applied after the first two convolutional layers. The extracted features are then passed through two fully connected layers for final classification. The model is trained for 10 epochs using Cross Entropy Loss and the Adam optimizer (learning rate = 0.0001, weight decay = 0.01).

In addition to posture classification, the system is also designed to detect imbalance status. Data collected from yoga practitioners are segmented into windows of 50 data points with a stride of 10 using MATLAB. Each segment is labeled with one of three imbalance statuses (steady, slight imbalance, or moderate imbalance) across 15 yoga postures. A HMS is employed to perform classification, integrating predictions from five candidate models via a soft voting strategy (Text S5, Supporting Information). The candidate models include a 1D-CNN, RF, linear SVM, RBF SVM, and LR. The 1D-CNN architecture consists of two convolutional layers with 64 and 128 filters (kernel size = 3, padding = 1), each followed by ReLU activation and max pooling, and two fully connected layers. The model takes raw plantar pressure sequences of shape (50, 32) as input and is trained for 10 epochs using Cross Entropy Loss and the Adam optimizer (learning rate = 0.0005, batch size = 64). The traditional models (LR, RF, linear SVM, and RBF SVM) are implemented using scikit-learn in Python. They are trained on flattened (50 × 32) input sequences. All models are evaluated using a 9:1 training-to-testing ratio.

For user identification, plantar pressure signals corresponding to different yoga postures are collected using the customized PCB. The structure is illustrated in Figure 5a. The model is trained for 10 epochs using Cross Entropy Loss and the Adam optimizer (learning rate = 0.0001, weight decay = 0.01). ReLU is used as the activation function. The model input consists of multi-channel plantar pressure sequences, and data from each user is split 8:2 for training and testing. To provide personalized guidance for yoga practitioners, four COP-based stability parameters are predicted using a multi-output random forest regression model, consisting of four individual regressors (n_estimators = 100, random_state = 42), implemented with scikit-learn in Python. The model structure is illustrated in Figure 5d. All machine learning models are developed using Python 3.11.13, with PyTorch 2.6.0+cu124 and CUDA 12.4.

Development of Haptic-Enhanced Immersive Yoga Training and the Metaverse-Enabled Yoga Coach Avatar: The haptic-enhanced immersive yoga training system is developed through the integration of hardware, AI-based data processing, and virtual guidance presentation. The haptic units are controlled by the MCU through varying applied voltage levels, and their displacement and frequency responses are characterized using a laser vibrometer (PDV-100, Polytec). Meanwhile, pressure data during yoga practice is collected using a customized PCB and wirelessly transmitted to a computer for processing. Under the same Python environment, the acquired pressure signals are analyzed using machine learning algorithms. Four COP-based stability parameters are predicted using the trained multi-output RF regression model and then compared with the corresponding ground-truth values of the yoga practitioners. The comparison results are sent to ChatGPT for personalized guidance. The process is realized based on the OpenAI developer platform (Python package OpenAI Application Programming Interface (API)), where the model is set to "gpt-4.1" for natural language generation. Then the generated guidance is sent to Unity 3D via Transmission Control Protocol/Internet Protocol (TCP/IP) communication, where it is visualized and mapped onto a metaverse-based yoga coach avatar for immersive guidance and correction.

Supporting Information

Supporting Information is available from the Wiley Online Library or from the author.

Acknowledgements

The work was supported by the RIE Advanced Manufacturing and Engineering (AME) Programmatic Grant (Grant A18A4b0055), RIE 2025 – Industry Alignment Fund – Industry Collaboration Projects (IAF-ICP) (Grant I2301E0027), Research Platform for Biomedical and Health Technology (RP-BTH-Prof. LEE Chengkuo) in NUS (Suzhou) Research Insititute, NUS College of Design and Engineering (CDE)-Robotics Seed Grant Programme, “AI-Sensor Enhanced Medical Operation Training System (A-8003283-00-00)”, NUS College of Design and Engineering (CDE)-Robotics Seed Grant Programme, “A Multimodal Sensing/ Haptic System For lower-Limb Exoskeleton Feedback Control (A-8003281-00-00)”. Special thanks to Mr. Abhijeet Pandey, Yoga Instructor, Ms. Patricia Lin Yi Hsi and Ms. Katherine Lee Meng Tzu, Yoga Practitioners, at Ayu Yoga, Singapore.

Conflict of Interest

The authors declare no conflict of interest.

Data Availability Statement

The data that support the findings of this study are available from the corresponding author upon reasonable request.

Keywords

hydrogel, machine learning, metaverse, multimodal sensing, smart insole

Received: July 31, 2025
Revised: October 10, 2025
Published online: October 22, 2025

[1] T. Leng, L. Li, C. Lee, *AI Sensors* **2025**, *1*, 1. https://doi.org/10.3390/aisens1010001.
[2] Z. Zhang, L. Wang, C. Lee, *Adv. Sens. Res.* **2023**, *2*, 2200072, https://doi.org/10.1002/adsr.202200072.
[3] D. Liu, D. Zhang, Z. Sun, S. Zhou, W. Li, C. Li, W. Li, W. Tang, Z. L. Wang, *Adv. Funct. Mater.* **2022**, *32*, 2113008. https://doi.org/10.1002/adfm.202113008.
[4] S. Chen, S. Fan, Z. Qiao, Z. Wu, B. Lin, Z. Li, M. A. Riegler, M. Y. H. Wong, A. Opheim, O. Korostynska, K. M. Nielsen, T. Glott, A. C. T. Martinsen, V. H. Telle-Hansen, C. T. Lim, *Adv. Mater.* **2025**, *37*, 2500412. https://doi.org/10.1002/adma.202500412.
[5] K. R. Pyun, K. Kwon, M. J. Yoo, K. K. Kim, D. Gong, W. H. Yeo, S. Han, S. H. Ko, *Natl. Sci. Rev.* **2024**, *11*, nwad298, https://doi.org/10.1093/nsr/nwad298.
[6] C. Wang, H. Niu, G. Shen, Y. Li, *Adv. Funct. Mater.* **2024**, *35*, 2419809.
[7] K. Meng, X. Xiao, W. Wei, G. Chen, A. Nashalian, S. Shen, X. Xiao, J. Chen, *Adv. Mater.* **2022**, *34*, 2109357.
[8] W. Di Li, K. Ke, J. Jia, J. H. Pu, X. Zhao, R. Y. Bao, Z. Y. Liu, L. Bai, K. Zhang, M. B. Yang, W. Yang, *Small* **2022**, *18*, 2103734.
[9] Y. Wang, L. Chu, S. Meng, M. Yang, Y. Yu, X. Deng, C. Qi, T. Kong, Z. Liu, *Adv. Sci.* **2024**, *11*, 2401436.
[10] D. Liu, D. Zhang, Z. Sun, S. Zhou, W. Li, C. Li, W. Li, W. Tang, Z. L. Wang, *Adv. Funct. Mater.* **2022**, *32*, 2113008.
[11] C. Deng, W. Tang, L. Liu, B. Chen, M. Li, Z. L. Wang, *Adv. Funct. Mater.* **2018**, *28*, 1801606. https://doi.org/10.1002/adfm.201801606.
[12] C. Zhao, J. Park, S. E. Root, Z. Bao, *Nat. Rev. Bioeng.* **2024**, *2*, 671. https://doi.org/10.1038/s44222-024-00194-1.
[13] Z. Du, L. Li, G. Shen, *Nano-Micro Lett.* **2025**, *17*, 204. https://doi.org/10.1007/s40820-025-01721-4.
[14] Y. Guo, K. Li, W. Yue, N.-Y. Kim, Y. Li, G. Shen, J.-C. Lee, *Nano-Micro Lett.* **2025**, *17*, 41. https://doi.org/10.1007/s40820-024-01545-8.
[15] X. Xiong, J. Liang, W. Wu, *Nano Energy* **2023**, *113*, 108542. https://doi.org/10.1016/j.nanoen.2023.108542.
[16] S. Sunwoo, S. I. Han, C. S. Park, J. H. Kim, J. S. Georgiou, S. Lee, D. Kim, T. Hyeon, *Nat. Rev. Bioeng.* **2023**, *2*, 8. https://doi.org/10.1038/s44222-023-00102-z.
[17] Q. Zheng, Q. Tang, Z. L. Wang, Z. Li, *Nat. Rev. Cardiol.* **2021**, *18*, 7. https://doi.org/10.1038/s41569-020-0426-4.
[18] F. Haghayegh, A. Norouziazad, E. Haghani, A. A. Feygin, R. H. Rahimi, H. A. Ghavamabadi, D. Sadighbayan, F. Madhoun, M. Papagelis, T. Felfeli, R. Salahandish, *Adv. Sci.* **2024**, *11*, 2400595. https://doi.org/10.1002/advs.202400595.
[19] K. Mahato, T. Saha, S. Ding, S. S. Sandhu, A. Chang, J. Wang, *Nat. Electron.* **2024**, *7*, 735. https://doi.org/10.1038/s41928-024-01247-4.
[20] S. Chen, Z. Qiao, Y. Niu, J. C. Yeo, Y. Liu, J. Qi, S. Fan, X. Liu, J. Y. Lee, C. T. Lim, *Nat. Rev. Bioeng.* **2023**, *1*, 950. https://doi.org/10.1038/s44222-023-00094-w.
[21] N. Brasier, J. Wang, W. Gao, J. R. Sempionatto, C. Dincer, H. C. Ates, F. Güder, S. Olenik, I. Schauwecker, D. Schaffarczyk, E. Vayena, N. Ritz, M. Weisser, S. Mtenga, R. Ghaffari, J. A. Rogers, J. Goldhahn, *Nature* **2024**, *636*, 57. https://doi.org/10.1038/s41586-024-08249-4.
[22] F. Wen, Z. Zhang, T. He, C. Lee, *Nat. Commun.* **2021**, *12*, 5378. https://doi.org/10.1038/s41467-021-25637-w.
[23] Y. Luo, Y. Li, P. Sharma, W. Shou, K. Wu, M. Foshey, B. Li, T. Palacios, A. Torralba, W. Matusik, *Nat. Electron.* **2021**, *4*, 193. https://doi.org/10.1038/s41928-021-00558-0.
[24] C. Xu, Y. Song, J. R. Sempionatto, S. A. Solomon, Y. Yu, H. Y. Y. Nyein, R. Y. Tay, J. Li, W. Heng, J. Min, A. Lao, T. K. Hsiai, J. A. Sumner, W. Gao, *Nat. Electron.* **2024**, *7*, 168. https://doi.org/10.1038/s41928-023-01116-6.
[25] D. Lee, J. Bae, *Adv. Funct. Mater.* **2024**, *34*, 2409841.
[26] W. Li, Z. Chen, C. Xu, X. Zhao, C. Ren, P. Wei, *Adv. Funct. Mater.* **2025**, 12653.
[27] J. Yang, K. Yang, X. An, Z. Fan, Y. Li, L. Yin, Y. Long, *Adv. Funct. Mater.* **2025**, *35*, 2416916.
[28] M. Chen, X. An, F. Zhao, P. Chen, J. Wang, M. Zhang, A. Lu, *Nano-Micro Lett.* **2025**, *17*, 205. https://doi.org/10.1007/s40820-025-01718-z.
[29] B. Ying, X. Liu, *iScience* **2021**, *24*, 103174. https://doi.org/10.1016/j.isci.2021.103174.
[30] R. Xu, T. Xu, M. She, X. Ji, G. Li, S. Zhang, X. Zhang, H. Liu, B. Sun, G. Shen, M. Tian, *Nano-Micro Lett.* **2025**, *17*, 90. https://doi.org/10.1007/s40820-024-01566-3.
[31] D. Han, Y. Cai, X. Wang, W. Zhang, X. Li, Z. Hou, J. Liu, D. Song, W. Xu, *Adv. Funct. Mater.* **2025**, *35*, 2501362.
[32] Z. Zhang, T. He, M. Zhu, Z. Sun, Q. Shi, J. Zhu, B. Dong, M. R. Yuce, C. Lee, *npj Flex. Electron.* **2020**, *4*, 29. https://doi.org/10.1038/s41528-020-00092-7.
[33] F. Wen, Z. Sun, T. He, Q. Shi, M. Zhu, Z. Zhang, L. Li, T. Zhang, C. Lee, *Adv. Sci.* **2020**, *7*, 2000261. https://doi.org/10.1002/advs.202000261.

[34] T. He, Z. Sun, Q. Shi, M. Zhu, D. V. Anaya, M. Xu, T. Chen, M. R. Yuce, A. V. Thean, C. Lee, *Nano Energy* **2019**, *58*, 641. https://doi.org/10.1016/j.nanoen.2019.01.091.

[35] L. Liu, T. Hu, X. Zhao, Y. Su, D. Yin, C. Lee, Z. L. Wang, *Nano Energy* **2025**, *133*, 110491. https://doi.org/10.1016/j.nanoen.2024.110491.

[36] M. Zhu, Z. Sun, C. Lee, *ACS Nano* **2022**, *16*, 14097. https://doi.org/10.1021/acsnano.2c04043.

[37] Y. Ma, J. Ouyang, T. Raza, P. Li, A. Jian, Z. Li, H. Liu, M. Chen, X. Zhang, L. Qu, M. Tian, G. Tao, *Nano Energy* **2021**, *85*, 105941. https://doi.org/10.1016/j.nanoen.2021.105941.

[38] Z. H. Guo, Z. Zhang, K. An, T. He, Z. Sun, X. Pu, C. Lee, *Research* **2023**, *6*, 0154, https://doi.org/10.34133/research.0154.

[39] S. Gao, T. He, Z. Zhang, H. Ao, H. Jiang, C. Lee, *Adv. Sci.* **2021**, *8*, 2105235. https://doi.org/10.1002/advs.202105235.

[40] A. K. Rajendran, S. C. Sethuraman, *IEEE Access* **2023**, *11*, 11183. https://doi.org/10.1109/ACCESS.2023.3240769.

[41] R. Govindaraj, S. Karmani, S. Varambally, B. N. Gangadhar, *Int. Rev. Psychiatry* **2016**, *28*, 242. https://doi.org/10.3109/09540261.2016.1160878.

[42] H. Cramer, L. Ward, A. Steel, R. Lauche, G. Dobos, Y. Zhang, *Am. J. Prev. Med.* **2016**, *50*, 230. https://doi.org/10.1016/j.amepre.2015.07.037.

[43] C. Wiese, D. Keil, A. S. Rasmussen, R. Olesen, *J. Bodyw. Mov. Ther.* **2019**, *23*, 479. https://doi.org/10.1016/j.jbmt.2018.09.151.

[44] M. Gochoo, T.-H. Tan, S.-C. Huang, T. Batjargal, J.-W. Hsieh, F. S. Alnajjar, Y.-F. Chen, *IEEE Internet Things J* **2019**, *6*, 7192. https://doi.org/10.1109/JIOT.2019.2915095.

[45] A. Gupta, H. P. Gupta, *IEEE Trans. Artif. Intell.* **2021**, *2*, 362. https://doi.org/10.1109/TAI.2021.3096175.

[46] S. W. Mohammed, V. Garrapally, S. Manchala, S. N. Reddy, S. K. Naligenti, *Int. J. Comput. Digit. Syst.* **2022**, *13*, 1295.

[47] L. Truppa, E. Bergamini, P. Garofalo, M. Costantini, C. Fiorentino, G. Vannozzi, A. M. Sabatini, A. Mannini, *IEEE Sens. J.* **2021**, *21*, 21285. https://doi.org/10.1109/JSEN.2021.3101295.

[48] S. Omkar, M. Mour, D. Das, *Int. J. Yoga* **2009**, *2*, 62. https://doi.org/10.4103/0973-6131.60046.

[49] A. Chaudhari, O. Dalvi, O. Ramade, D. Ambawade, Proceedings – International Conference on Communication, Information & Computing Technology (ICCICT), IEEE, **2021**.

[50] S. Jain, A. Rustagi, S. Saurav, R. Saini, S. Singh, *Neural Comput. Appl.* **2021**, *33*, 6427. https://doi.org/10.1007/s00521-020-05405-5.

[51] S. K. Yadav, A. Singh, A. Gupta, J. L. Raheja, *Neural Comput. Appl.* **2019**, *31*, 9349. https://doi.org/10.1007/s00521-019-04232-7.

[52] T. K. K. Maddala, P. V. V. Kishore, K. K. Eepuri, A. K. Dande, *IEEE Trans. Multimed.* **2019**, *21*, 2492. https://doi.org/10.1109/TMM.2019.2904880.

[53] M. C. Thar, K. Z. N. Winn, N. Funabiki, presented at *2019 Int. Conf. on Advanced Information Technologies (ICAIT)*, Yangon, Myanmar, November **2019**.

[54] S. Datta, in *Evolution and Interconnection: Geometry in Early Temple Architecture*, Springer, New York **2020**.

[55] Y. Wu, Q. Lin, M. Yang, J. Liu, J. Tian, D. Kapil, L. Vanderbloemen, *Healthcare* **2022**, *10*, 36.

[56] R. J. Doyle, E. T. Hsiao-Wecksler, B. G. Ragan, K. S. Rosengren, *Gait Posture* **2007**, *25*, 166. https://doi.org/10.1016/j.gaitpost.2006.03.004.

[57] A. Ruhe, R. Fejer, B. Walker, *Eur. Spine J.* **2011**, *20*, 358.

[58] V. Krishnamoorthy, M. L. Latash, J. P. Scholz, V. M. Zatsiorsky, *Exp. Brain Res.* **2003**, *152*, 281. https://doi.org/10.1007/s00221-003-1574-6.

[59] I. Almuteb, R. Hua, Y. Wang, *Smart Health* **2022**, *25*, 100301. https://doi.org/10.1016/j.smhl.2022.100301.

[60] S. Subramaniam, S. Majumder, A. I. Faisal, M. J. Deen, *Sensors* **2022**, *22*, 438. https://doi.org/10.3390/s22020438.

[61] X. Wu, Y. Khan, J. Ting, J. Zhu, S. Ono, X. Zhang, S. Du, J. W. Evans, C. Lu, A. C. Arias, *Adv. Electron. Mater.* **2020**, *6*, 1901310, https://doi.org/10.1002/aelm.201901310.

[62] B. Baro, S. Khimhun, U. Das, S. Bayan, *Nano Energy* **2023**, *108*, 108212. https://doi.org/10.1016/j.nanoen.2023.108212.

[63] R. M. Stess, S. R. Jensen, R. Mirmiran, *Diabetes Care* **1997**, *20*, 855. https://doi.org/10.2337/diacare.20.5.855.

[64] C. Payne, D. Turner, K. Miller, *J. Diabetes Complications* **2002**, *16*, 277. https://doi.org/10.1016/S1056-8727(01)00187-8.

[65] S. Saidani, R. Haddad, N. Mezghani, R. Bouallegue, presented at *2018 International Conference on Smart Communications and Networking (SmartNets)*, Yasmine Hammamet, Tunisia, November **2018**.

[66] C. Herbers, R. Zhang, A. Erdman, M. D. Johnson, *npj Park. Dis.* **2024**, *10*, 67, https://doi.org/10.1038/s41531-024-00678-2.

[67] R. Okuno, S. Fujimoto, J. Akazawa, M. Yokoe, S. Sakoda, K. Akazawa, in *Proceedings of 30th Annual International Conference of the IEEE Engineering in Medicine and Biology Society EMBS'08 – "Personalized Healthcare through Technology*, IEEE, Piscataway, NJ, **2008**, p. 1765.

[68] S. Hu, H. Li, W. Lu, T. Han, Y. Xu, X. Shi, Z. Peng, X. Cao, *Adv. Funct. Mater.* **2024**, *34*, 2313458.

[69] Y. Tian, L. Zhang, C. Zhang, B. Bao, Q. Li, L. Wang, Z. Song, D. Li, *Exploration* **2024**, *4*, 20230109, https://doi.org/10.1002/EXP.20230109.

[70] L. Song, Z. Wang, S. Chen, Y. Shen, J. Yin, R. Wang, *Adv. Mater.* **2025**, *37*, 2417978. https://doi.org/10.1002/adma.202417978.

[71] F. Xiao, Z. Wei, Z. Xu, H. Wang, J. Li, J. Zhu, *Adv. Sci.* **2025**, *12*, 2410284.

[72] J. Tao, M. Dong, L. Li, C. Wang, J. Li, Y. Liu, R. Bao, C. Pan, *Microsyst. Nanoeng.* **2020**, *6*, 62. https://doi.org/10.1038/s41378-020-0171-1.

[73] W. Li, K. Zou, J. Guo, C. Zhang, J. Feng, J. You, G. Cheng, Q. Zhou, M. Kong, G. Li, C. F. Guo, J. Yang, *ACS Nano* **2024**, *18*, 14672. https://doi.org/10.1021/acsnano.4c02919.

[74] Q. Wang, H. Guan, C. Wang, P. Lei, H. Sheng, H. Bi, J. Hu, C. Guo, Y. Mao, J. Yuan, M. Shao, Z. Jin, J. Li, W. Lan, *Sci. Adv.* **2025**, *11*, adu1598 https://doi.org/10.1126/sciadv.adu1598.

[75] X. Li, X. Liu, W. Zeng, D. Ding, B. Liu, Y. Li, Z. Zhao, S. Zhan, W. Zhu, Z. Chen, J. Huang, J. Luo, *Adv. Mater. Technol.* **2023**, *8*, 2300095. https://doi.org/10.1002/admt.202300095.

[76] H. Zhou, Y. Gui, G. Gu, H. Ren, W. Zhang, Z. Du, G. Cheng, *Small* **2025**, *21*, 2405064.

[77] S. Hu, H. Li, W. Lu, T. Han, Y. Xu, X. Shi, Z. Peng, X. Cao, *Adv. Funct. Mater.* **2024**, *34*, 2313458. https://doi.org/10.1002/adfm.202313458.

[78] W. Wang, J. Cao, J. Yu, R. Liu, C. R. Bowen, W.-H. Liao, *Sensors* **2019**, *19*, 5336. https://doi.org/10.3390/s19245336.

[79] X. Guo, L. Wang, Z. Jin, C. Lee, *Nano-Micro Lett.* **2025**, *17*, 76. https://doi.org/10.1007/s40820-024-01587-y.

[80] Z. Sun, Z. Zhang, C. Lee, *Nat. Electron.* **2023**, *6*, 941. https://doi.org/10.1038/s41928-023-01093-w.

[81] Z. Sun, M. Zhu, X. Shan, C. Lee, *Nat. Commun.* **2022**, *13*, 5224. https://doi.org/10.1038/s41467-022-32745-8.

[82] L. Wang, M. Xiao, X. Guo, Y. Yang, Z. Zhang, C. Lee, *Biosensors* **2024**, *14*, 629. https://doi.org/10.3390/bios14120629.

[83] Z. Zhang, X. Guo, C. Lee, *Nat. Commun.* **2024**, *15*, 6465. https://doi.org/10.1038/s41467-024-50261-9.

[84] Z. Sun, T. He, Z. Ren, C. Wang, X. Liu, Z. Zhang, J. Zhou, X. Guo, Y. Yang, C. Lee, *SmartSys* **2025**, *1*, 4.

[85] X. Guo, Z. Sun, Y. Zhu, C. Lee, *Adv. Mater.* **2024**, *36*, 2406778. https://doi.org/10.1002/adma.202406778.

[86] F. R. P. G. Rogerio, D. P. Guedes, *Fisioter. Mov.* **2022**, *35*, e35137. https://doi.org/10.1590/fm.2022.35137.

[87] Y. Xu, E. De la Paz, A. Paul, K. Mahato, J. R. Sempionatto, N. Tostado, M. Lee, G. Hota, M. Lin, A. Uppal, W. Chen, S. Dua, L. Yin, B. L. Wuerstle, S. Deiss, P. Mercier, S. Xu, J. Wang, G. Cauwenberghs, *Nat. Biomed. Eng.* **2023**, *7*, 1307. https://doi.org/10.1038/s41551-023-01095-1.

[88] R. Jayawardena, P. Ranasinghe, H. Ranawaka, N. Gamage, D. Dissanayake, A. Misra, *Int. J. Yoga* **2020**, *13*, 99. https://doi.org/10.4103/ijoy.IJOY_37_19.

[89] A. Harris, M. Austin, T. M. Blake, M. L. Bird, *Complement. Ther. Clin. Pract.* **2019**, *34*, 153. https://doi.org/10.1016/j.ctcp.2018.11.015.

[90] K. Xiang, M. Liu, J. Chen, Y. Bao, Z. Wang, K. Xiao, C. Teng, N. Ushakov, S. Kumar, X. Li, R. Min, *ACS Appl. Mater. Interfaces* **2024**, *16*, 32662. https://doi.org/10.1021/acsami.4c04467.

[91] W. Li, R. Min, D. Zheng, Y. Long, K. Xiao, Z. Wang, M. Guo, Q. Chen, L. Liu, X. Li, Z. Li, *ACS Appl. Mater. Interfaces* **2025**, *17*, 11126. https://doi.org/10.1021/acsami.4c21754.

[92] W. Li, Y. Long, Y. Yan, K. Xiao, Z. Wang, D. Zheng, A. Leal-junior, S. Kumar, B. Ortega, C. Marques, X. Li, R. Min, W. Li, Y. Long, Y. Yan, K. Xiao, Z. Wang, D. Zheng, A. Leal-junior, S. Kumar, *Opto-Electron. Adv.* **2025**, *8*, 240254. https://doi.org/10.29026/oea.2025.240254.

[93] L. Shu, T. Hua, Y. Wang, Q. Li, D. D. Feng, X. Tao, *IEEE Trans. Inf. Technol. Biomed.* **2010**, *14*, 767.

[94] F. Lin, A. Wang, Y. Zhuang, M. R. Tomita, W. Xu, *IEEE Trans. Ind. Inform.* **2016**, *12*, 2281. https://doi.org/10.1109/TII.2016.2585643.

[95] S. Fujii, Y. Takamura, K. Ikuno, S. Morioka, N. Kawashima, *J. Neuroeng. Rehabil.* **2024**, *21*, 59. https://doi.org/10.1186/s12984-024-01358-1.

[96] X. Guo, Z. Zhang, Z. Ren, D. Li, C. Xu, L. Wang, W. Liu, *Adv. Mater.* **2025**, 10417. https://doi.org/10.1002/adma.202510417.

[97] X. Zhou, D. Li, S. He, M. Xiao, Z. Sui, F. Zha, L. Sun, C. Lee, H. Liu, *SmartBot* **2025**, *1*, 70004.

[98] L. Xu, L. Li, T. Wang, S. Yi, C. Zhang, *InfoMat* **2025**, 70086. https://doi.org/10.1002/inf2.70086.